Post-Print

Experimental Investigation of the Rotor-Wing Aerodynamic Interaction in a Tiltwing Aircraft in Hover

G.Droandi, A.Zanotti, G.Gibertini, D.Grassi and G.Campanardi

Dipartimento di Scienze e Tecnologie Aerospaziali

Politecnico di Milano, Campus Bovisa, Via La Masa 34, 20156 Milano, Italy

e-mail: giovanni.droandi@polimi.it

Abstract

The hovering performance and the lifting capability of tiltrotor aircraft are strongly affected by the aerodynamic interaction between wing and rotors. The tiltwing concept represents a promising technology to increase the hover performance by reducing the wing-rotor interference. The present work describes an experimental activity carried out on a 1/4 scaled tiltwing aircraft half-model to achieve a detailed insight about the main issues characterising the aerodynamic interaction between wing and rotor in hover. The results of the experimental campaign, including both force measurements and Particle Image Velocimetry surveys, enabled to evaluate both the aircraft performance for different configurations of the tilting wing and to achieve a detailed insight about the flow physics of the rotor wake in the interaction with the wing. The test activity provided a comprehensive experimental database that was obtained over a not confidential aircraft configuration.

Nomenclature

A	rotor disk area, πR^2
c	blade chord
C_P	power coefficient, $P/(\rho A \Omega^3 R^3)$
C_T	thrust coefficient, $T/(\rho A \Omega^2 R^2)$
$C_{T\star}$	net thrust coefficient, $(T - F_z^w)/(\rho A \Omega^2 R^2)$
FM	figure of merit, $C_T^{3/2}/(C_P \sqrt{2})$
$FM^\star$	net figure of merit, $C_{T\star}^{3/2}/(C_P \sqrt{2})$
F	aerodynamic force
h	vertical distance between the wing rotation axis and the rotor disk
M	Mach number
P	rotor power
N_b	number of blades
r	radial coordinate
R	rotor radius
Re	Reynolds number
U	velocity component
T	rotor thrust
x	longitudinal coordinate
y	span-wise coordinate
z	vertical coordinate
τ	tilted wing angle
ρ	air density
σ	rotor solidity, $cN_b/(\pi R)$
θ	collective pitch angle
ψ	azimuthal angle position
Ω	rotational frequency of rotor
Superscript:	
w	relative to half-wing
Subscript:	
tip	relative to blade tip
v	relative to the vortex core centre
x	longitudinal direction
y	span-wise direction
z	vertical direction

1 Introduction

A tiltrotor is an aircraft that combines the capability to hover, typical of helicopters, and the possibility to flight in cruise at high speed, like propeller driven aircraft. The tiltrotor concept represents a concrete possibility to overcome the main limitations of helicopters and propeller aircraft by matching their respective peculiarities. Thanks to the high versatility of this kind of aircraft[1,2], the tiltrotor concept represents nowadays a very attractive compromise for the civil industry. However, the hovering performance and the lifting capability of this kind of aircraft are strongly affected by the aerodynamic interaction between wing and rotors. In helicopter flight mode, the presence of the wing under the rotor significantly modifies the rotor wake and thus it is responsible for loss of rotor performance[3]. As already described by McVeigh[4] and by Felker and Light[5], when the wing is taken into account, the rotor performance change with respect to the isolated case. In particular, as shown by McCluer and Johnson[6] for the Full-Span Tiltrotor Aeroacoustic Model (FS-TRAM), the rotor FM is strongly affected by the presence of the airframe and considerably decreases with respect to the isolated rotor case[7]. Moreover, when the rotor wake impinges on the wing surface a download force, that is approximately 10%-15% of the rotor thrust[4.8], is generated. In order to overcome these limitations in the actual tiltrotors (XV-15, V-22 Ospray and BA609) large rotors were adopted, although this solution increased the aerodynamic interference due to wing-rotor[9] and rotor-rotor[10] interaction. Moreover, large rotors prevent the take-off and landing in aircraft flight mode and lead to important limitations in cruise flight, such as the maximum cruise speed achieved and the operative range, which is limited by a relevant fuel consumption.

Since the improvement of the performance in aircraft mode is actually one of the focus points for future developments of new tiltrotor aircraft, non-conventional tiltrotor configurations have to be further investigated[11,12] with the aim to preserve the performance in helicopter mode. A possible approach to improve the performance in aircraft mode (i.e. the propulsive efficiency and the cruise speed) is to modify significantly the blade shape[13] reducing the rotor diameter in order to get a propeller similar to the aircraft ones[14]. This solution leads to the tiltwing concept that was recently adopted for the development of the European project ERICA (Enhanced Rotorcraft Innovative Concept Achievement[11]). The main characteristic of a tiltwing aircraft is represented by the possibility to tilt the external part of the wing with the rotor, minimising the wing surface on which the rotor wake strikes. Good hover performance is preserved and the resulting download force is less than 1% of the rotor thrust[15,16]. Even if the ERICA tiltrotor was the object of several experimental and numerical studies during the last fourteen years[17,18], many aspects of this aircraft configuration have to be further analysed. A detailed investigation of this promising solution would help engineers during

the design process of a tiltrotor aircraft. In particular, a correct characterisation of the rotor wake geometry together with a description of the flow field between the rotor plane and the wing would be useful to understand the phenomena related to the wing-rotor interaction. Nevertheless, experimental and numerical databases on tiltwing aircraft are very few and not public. On the other hand, many experimental works were done in the last few years on tiltrotors with conventional configuration. For example, Darabi et al.[3] gave descriptions of the mean and time-dependent rotor wake flow over a XV-15 tiltrotor model in hover using stereoscopic PIV, while Grife et al.[19] proposed the use of active flow control to reduce hover download on a scaled V-22 model.

In this framework, a research activity started at Dipartimento di Scienze e Tecnologie Aerospaziali (DSTA) of Politecnico di Milano to study the aerodynamic interference between wing and rotor on a high-performance tiltwing aircraft. A tiltwing aircraft in the same class of ERICA was defined by means of a statistical approach[15] and numerical calculations were used to get a first insight on the problem. A 1/4 scaled wind tunnel half-model[16] was designed in order to investigate the hovering flight condition. The present work describes the results of a comprehensive experimental campaign carried out on the tiltwing half-model to achieve a detailed insight about the aerodynamic interaction between the rotor and the wing in hover. In particular, both the aircraft performance and rotor wake geometry were investigated by means of force measurements and Particle Image Velocimetry (PIV) surveys.

2 Experimental set up

A new experimental test rig was designed and manufactured in the DSTA Aerodynamics Laboratory to study the aerodynamic interaction between wing and rotor in a tiltwing aircraft in hover flight condition. The test rig allows to investigate the sensibility of the aircraft performance to different parameter, as for instance the wing configuration and the vertical distance between the wing and the rotor disk.

2.1 Tiltwing half-model

A geometrical scale of 1/4 with respect to the full-scale aircraft was selected to design the experimental model[15,20]. The test rig consisted of two main components: the rotor system and the half-wing with an image plane. The two main systems are not linked in any parts in order to measure the rotor and the wing loads separately. Therefore, the rig enables also tests on the isolated rotor. Figure 1 shows the frontal and lateral views of the test rig as well as the cartesian $x - y - z$ model reference system. The origin of the reference system is the intersection point between the rotor shaft axis (z-axis) and
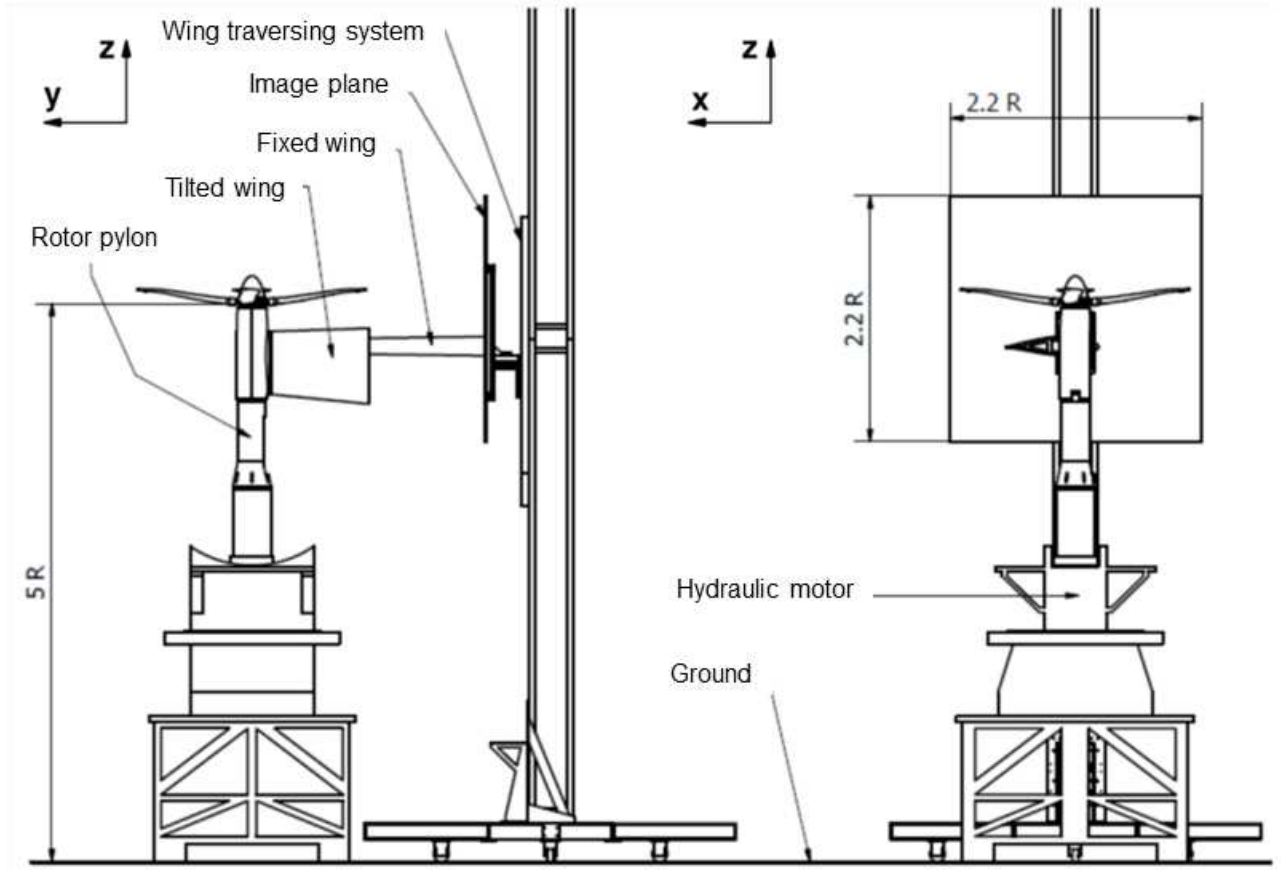
the rotor disk.

Figure 1: Schematic view of the experimental test rig and coordinate axis of the Cartesian $x - y - z$ reference system.

The four blades rotor has a radius of $R = 0.925\ m$. The design of the aerodynamic blade shape was carried out making use of a multi-objective optimisation procedure adopted in the frame of genetic optimisation techniques. A detailed description of the shape optimisation procedure is given in Droandi and Gibertini[21]. The main geometrical parameters of the rotor blade are summarised in Table 1. The thrust requirements for the rotor design were defined on the base of estimated values of the aircraft weight and drag obtained by means of classical preliminary design approach[15]. A complete description of the geometrical and structural characteristics of the rotor blade model is given in Droandi's doctoral dissertation[20].

The collective, longitudinal and lateral pitch controls are provided to the blades by means of three independent electric actuators acting on the swashplate. Each electric actuator is equipped with a linear potentiometer providing the feedback signal on the actual position of each command. The rotor hub is fully articulated and it is equipped with flap, led-lag and pitch hinges. Each blade hinge is

Section	r/R	c/R	Twist [deg]	Sweep [deg]	Airfoil
1	0.216	0.131	9.061	0.0	NACA 0030
2	0.270	0.133	8.351	0.0	NACA 0020
3	0.324	0.144	8.324	0.0	NACA 23014
4	0.487	0.168	5.217	−4.2	VR–5
5	0.649	0.179	−0.005	−4.4	OA–213
6	0.757	0.155	−2.265	−4.7	VR–7
7	0.865	0.154	−2.849	23.9	VR–5
8	0.946	0.131	−3.540	26.0	RC–510
9	1.000	0.108	−4.759	27.3	RC–510

Table 1: Geometric parameters of the rotor blade.

instrumented with a high accuracy Hall effect sensor to measure directly the pitch, led-lag and flap angles. A schematic view of the rotor hub is shown in Figure 2.
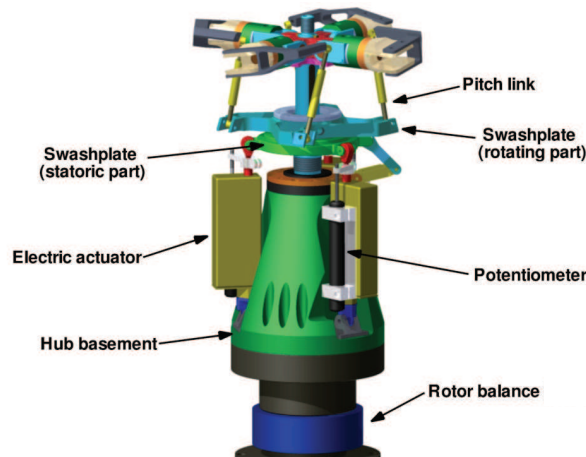

Figure 2: Detailed sketch of the four bladed rotor hub.

The rotor is powered by an hydraulic motor (maximum power 16 kW at 3000 rpm) located inside a swiveling base positioned on an aluminium base. The rotor disk is positioned at an height of 5 R from the ground. The rotor hub is mounted on a rigid pylon located over the hydraulic motor. A 24-channel slip ring is used for the transmission of electrical power and measurement signals from and to the rotating part of the rotor hub. A Hall Effect Sensor was employed to measure the rotational speed of the rotor and to trigger the PIV images acquisition with a prescribed azimuthal position of the blade. A hollow six-component strain gauge balance is embedded in the upper part of the pylon

under the rotor hub. A hollow shaft, passing through the balance, is instrumented with strain gauges to measure the rotor torque. This instrumented shaft is directly linked to the rotor hub shaft by a motoring coupling and to the transmission shaft by a torsionally stiff steel laminae coupling. The complete system was checked by means of reference weights and a maximum error of 0.5 N was found. The nacelle, manufactured in carbon fiber, has an external maximum diameter of 0.27 R and it is not weighted by the balance. The air intake is not present on the nacelle model as this feature was not taken into account in this study.

The half-wing model has a total span of 1.90 R and it is composed of two parts. The inner part, with 1.01 R span, is fixed while the outer part can rotate around the axis at 25 % of the local chord from $\tau = 0°$ (untilted configuration) to $\tau = 90°$ (tilted configuration). The wing is linearly tapered, untwisted with NACA 64A221 airfoil cross–section planes[22,23]. The airfoil chord is 0.75 m at the wing root and 0.52 m at the tip. The root section of the wing lies on the aircraft symmetry plane. The internal structure of both wing parts is made of extruded polystyrene foam with aluminium formers at the extremities. The external skin of the wing was made by a 2-layers carbon fiber skin. The wing is mounted on an independent vertical traversing system. Forces and moments on the wing were measured by a seven-component strain gauge balance located at the wing root. A square image plane with 2.2 R side is positioned at the fixed wing root to restore the symmetry condition on the symmetry plane of the model[8,10]. The image plane is fixed on the support of the wing traversing system. The upper side of the image plane is positioned at a distance of 0.9 R from the rotor disk. Further details about the tiltwing model set up are given in Droandi's doctoral dissertation[20].

2.2 PIV set up

The flow physics of the phenomena related to the aerodynamic interaction between the rotor wake and the wing was investigated by means of 2C PIV surveys carried out for both the isolated rotor and the half-model with the tilted wing. The employed PIV instrumentation[24] is composed by a Nd:YAG double pulsed laser with 200 mJ output energy and a wavelength of 532 nm and a double shutter CCD camera with a 12 bit, 1952×1112 pixel array. The camera was mounted on a single axis traversing system to move the measurement window in vertical direction (see Figure 3). The laser was alternatively mounted below the rotor disk to light a plane at x-constant (see Figure 4) and in front of the tilted wing to light different planes along the wing span at y-constant (cross–section planes). The x-constant plane represents an azimuthal plane for the isolated rotor configuration only.
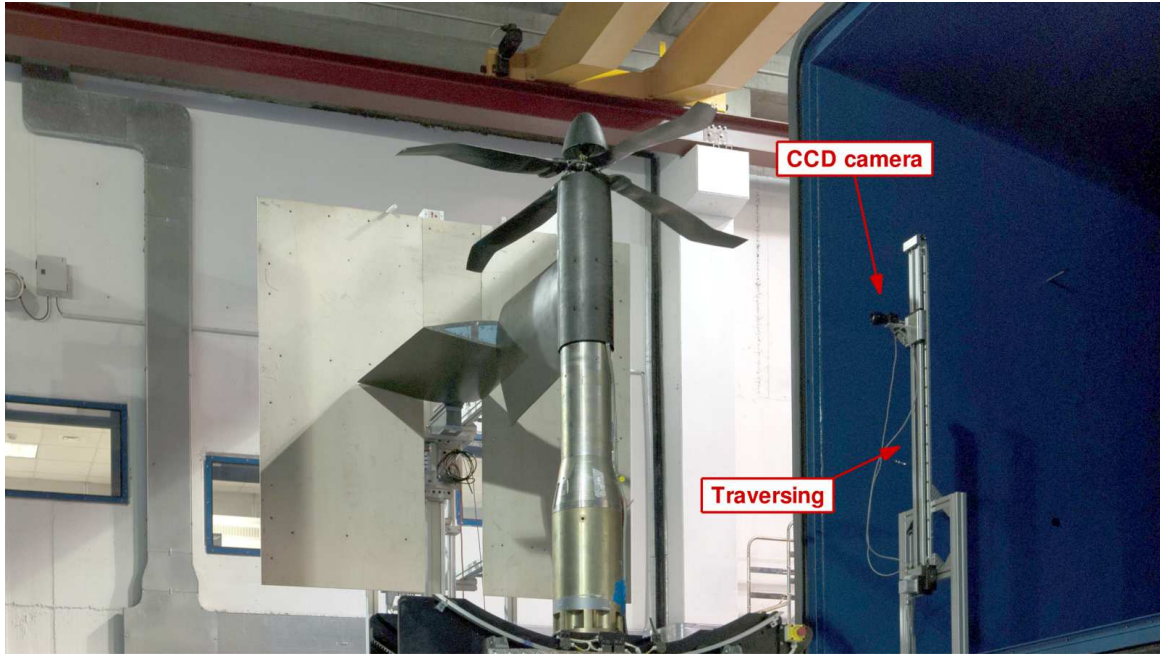
Figure 3: Experimental test rig for hovering tests in the open test section of the Politecnico di Milano Large Wind Tunnel.

In particular, an azimuthal measurement plane was considered for the isolated rotor tests perpendicular to the rotor disk (see Figure 5a). In order to avoid the interference of the light sheet with the tilted wing, the measurement plane for the half-model configuration is shifted by $x = -0.073\ m$ with respect to the isolated rotor test case (see Figure 5b). The PIV measurement area on the azimuthal plane for the isolated rotor was $0.38\ R$ wide and $0.90\ R$ high while for the half-model configurations the measurement area on the x-constant plane was $0.38\ R$ wide and $0.63\ R$ high. In order to achieve better resolution of the image pairs, the measurement area was composed respectively by four and three adjacent windows. A small band at the edges of the adjacent measurement windows overlapped with each other to obtain a better reconstruction of the overall flow field by averaging the shared field values. The lateral edge of the measurement area is aligned with the tilt-wing section while the upper edge is located at $z = 0.15\ R$. y-constant planes at $r/R = 0.69$ and $r/R = 0.79$ were surveyed only for the half-model configuration to evaluate the swirl in the rotor wake flow over the leading edge of the tilted wing. For this test case, the PIV measurement area was $0.27\ R$ wide and $0.30\ R$ high, and was composed by three adjacent windows with a small overlapping band between them (see Figure 5b). Phase-locked PIV measurements were carried out by synchronising the laser pulses with a prescribed azimuthal position of a selected rotor blade. The synchronisation of the PIV instrumentation was controlled by a 6 channels pulse generator. A particle generator with Laskin atomiser nozzles was used

Figure 4: Particular of the PIV set up on the test rig.

for the seeding. The image pairs post-processing was carried out using the PIVview 2C software[25] developed by PIVTEC. Multigrid technique[26] was employed to correlate the image pairs, up to an interrogation window of 32×32 pixels.

3   Test results and discussion

During the tests, the nominal rotational speed of the rotor, which rotates in anti-clockwise direction, was 1120 rpm. Although the declared maximum power of the hydraulic pump which drove the motor was 16 kW, the power given to the rotor was limited by the motor capacity. Therefore, the maximum power achieved during all the tests was about 8.5 kW corresponding to a maximum collective pitch of $\theta = 13.4°$. The tip Mach number was $M_{tip} = 0.32$ which correspond to half the tip Mach number of a full-scale aircraft at design point in hover. The authors are aware that some differences with respect to full-scale can, in principle, be expected due to Mach number effects (as well as to Reynolds
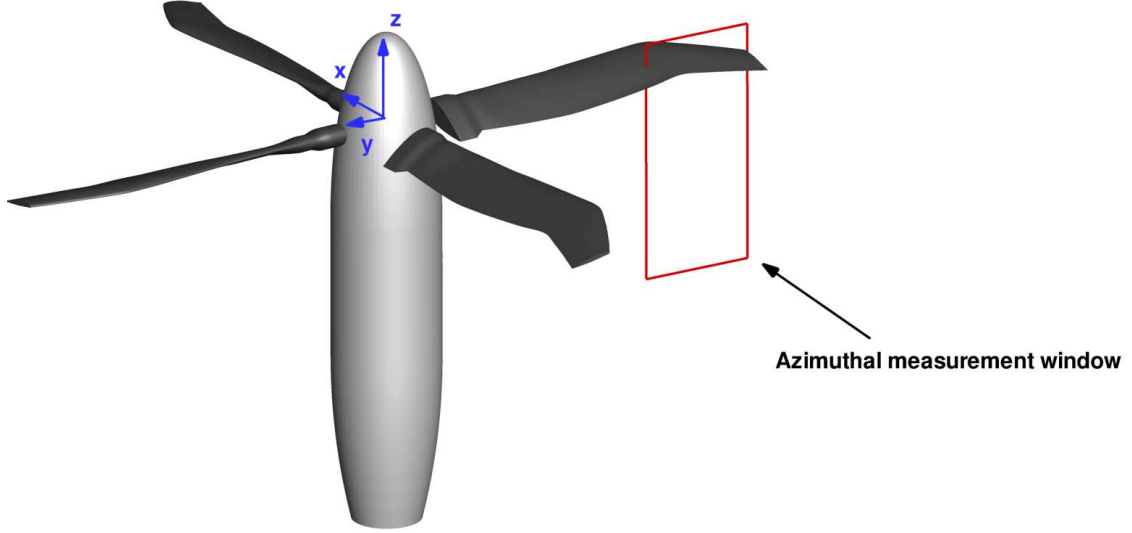
(a) Isolated rotor
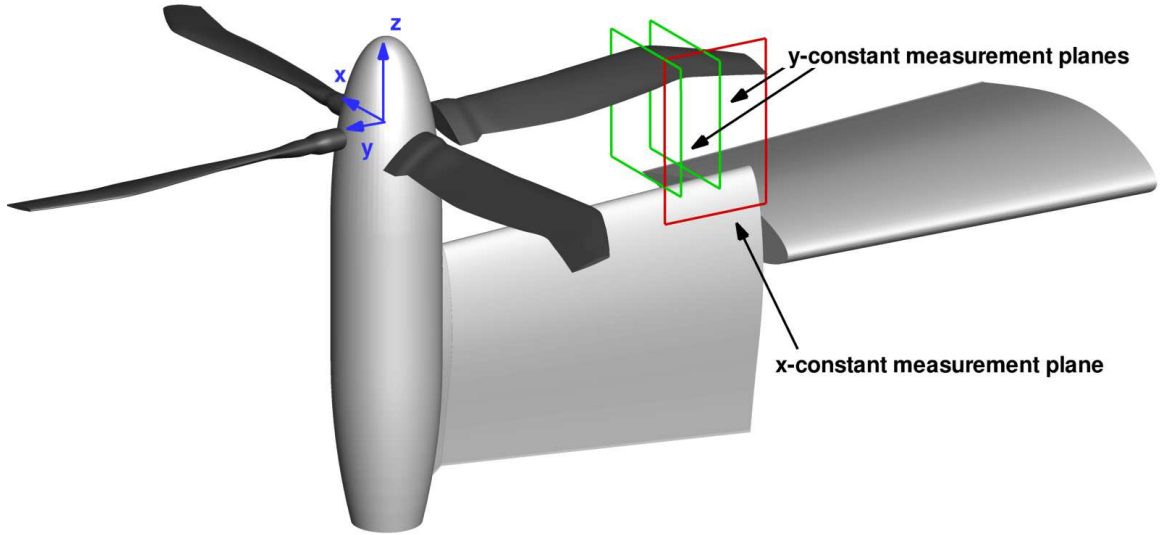
(b) Tiltwing half-model

Figure 5: Schematic view of the PIV planes.

number effects) but several previous works published by other authors[3,4,10,19] support the idea that the behaviour of the rotor wake flow is essentially the same.

Indeed, the Re_{Tip} number on the model (9.87×10^5) is lower with respect to the full-scale aircraft (7.89×10^6) but higher enough to reproduce the correct behaviour of the airfoils at the considered operative conditions. In fact, the angles of attack of the blade sections, as can be estimated by a blade element analysis, are always below the stall limit, so that a strong Reynolds sensibility is not expected. A higher effect could be expected for the Mach number, as the full-scale M_{tip} is equal to

0.64 so that the compressibility effects are not negligible. On the other hand, it can be pointed out that the operative condition is below the airfoil drag rise onset. As a confirmation of this, the rotor FM computed by Droandi[20] by means of a compressible Navier-Stokes analysis both in full-scale and experimental model conditions showed negligible differences. With respect to the effects on the wing, the Reynolds number is still large enough to avoid remarkable Reynolds effects.

The test activity started with the isolated rotor in order to characterise the performance of the rotor without the wing. Then, the rotor-wing aerodynamic interaction was investigated considering the wing at two different vertical distances with respect to the rotor disk (h). In particular, the tests were carried out with the wing positioned with its rotation axis at $z/R = -0.465$ and $z/R = -0.681$.

3.1 Force measurements

Figure 6a shows the behaviour of the isolated rotor FM as function of C_T/σ, while the measured power coefficient C_P trend is shown in Figure 6b as function of C_T. The error bars corresponds to twice the measurement standard deviation. The maximum value of FM achieved during these tests was 0.71 and it was obtained for $C_T = 0.0178$ and for $C_P = 0.0023$. However, the maximum value of C_T achieved during the experiments was 0.0180 because a further increase of collective pitch angle leaded to a power requirement over the motor capability. This value is lower than the thrust coefficient $C_T = 0.0215$ considered for the hovering condition in the design of the blade shape[21].

After the isolated rotor tests, the wing was introduced in the test rig. In order to evaluate the real efficiency of the aircraft system the resulting net thrust was considered as the difference between the rotor thrust and the wing load produced by the rotor wake ($T - F_z^w$).

The untilted ($\tau = 0°$) and the tilted ($\tau = 90°$) wings were tested to investigate how the airframe affects the rotor performance in hover. Figure 7a shows the behaviour of the rotor net figure of merit, $FM^\star$, as function of the ratio between the net thrust coefficient and the rotor solidity, $C_{T\star}/\sigma$. Figure 7b shows the rotor performance in terms of C_P as function of the net thrust coefficient, $C_{T\star}$. The tests results are compared in these figures with the isolated rotor data. In particular, it is apparent that the net aircraft system performance with the tilted wing is similar to the isolated rotor as the wing download is drastically reduced. On the other hand, with the untilted wing the power required by the aircraft to hover is much higher than in the isolated rotor case. The maximum C_P increment measured was about 26 % at $C_{T\star} = 0.014$ for both the lower and upper wing positions. This feature is due to the remarkable download produced by rotor wake on the wing, significantly decreasing the net aircraft system thrust in the order of 20 %. This value could be partially reduced by flap deflection as done in existing tiltrotor aircraft. For instance, Young et al.[27] found a download of about 16 % of the
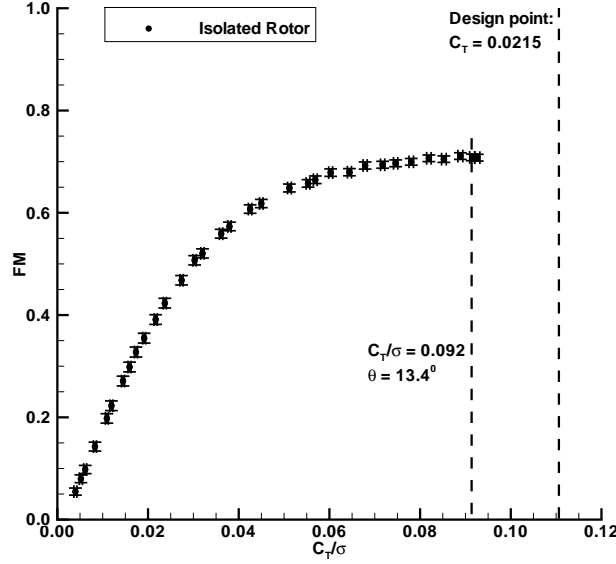
(a)
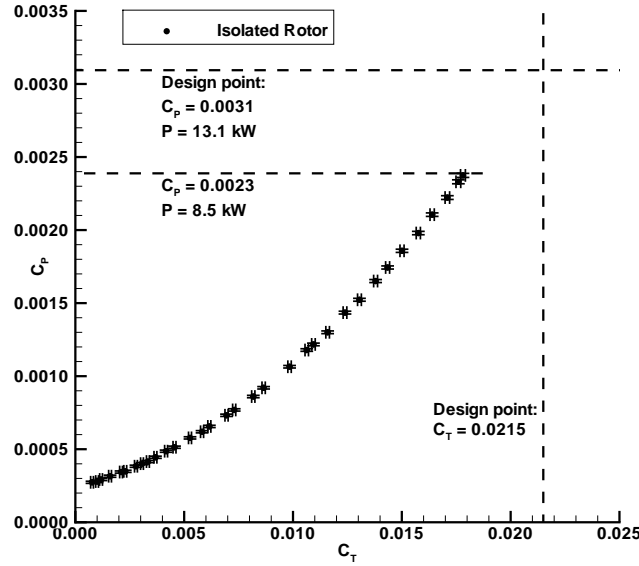
(b)

Figure 6: Isolated rotor performance: (a) FM as function of C_T/σ, (b) C_P as function of C_T, $M_{Tip} = 0.32$.

thrust for the V-22 full-span model. Figure 8 illustrates the rotor performance considering the thrust measured by the rotor balance for the different configurations tested. In particular Figure 8b shows that with the untilted wing the rotor experiences a partial ground effect producing a slight improvement of the rotor performance. Indeed, the value of thrust measured for the untilted configuration are slightly higher with respect to both the isolated rotor case and the tilted wing configuration for a given value of power (respectively about 2 % and 1 % more for $C_P > 0.0015$).
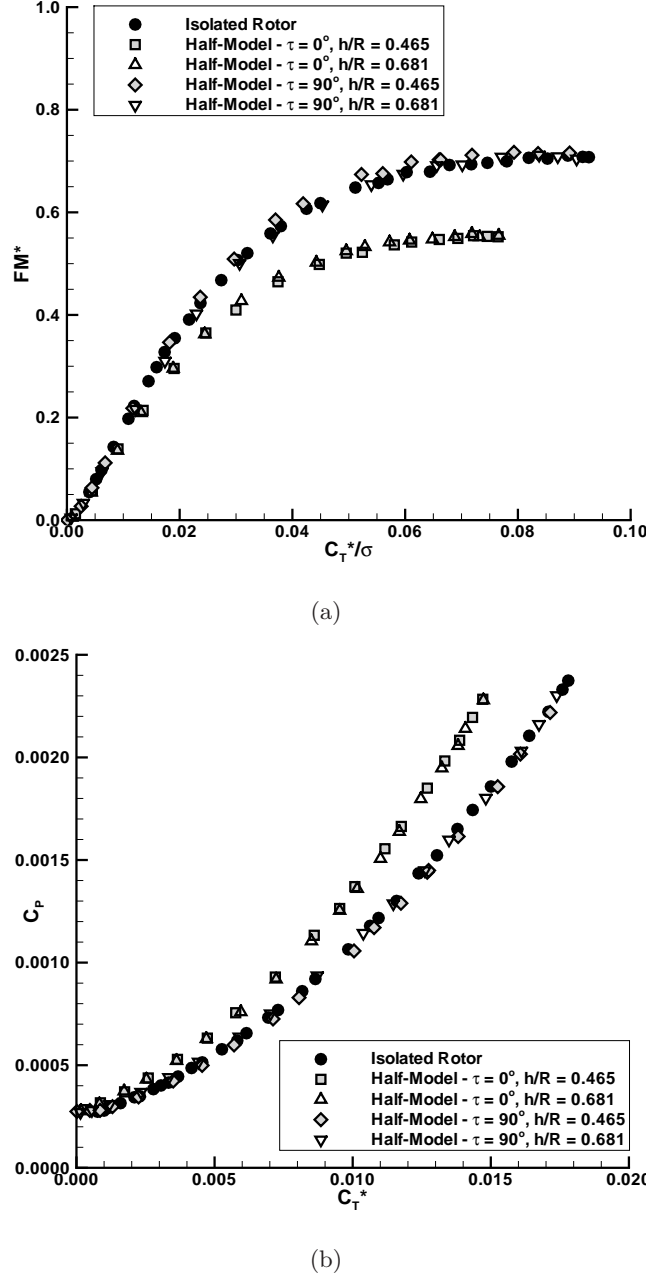
(a)

(b)

Figure 7: Comparison of aircraft system and isolated rotor performance, $M_{Tip} = 0.32$.

On the other hand, the tilted wing cases show a very different trend. In fact, the experimental results show a remarkable decrease of the power requirement. This feature is due to the drastic reduction of the vertical load F_z^w acting on the wing, as shown in Figure 9a. In particular, the vertical force/thrust ratio results less than 1 % for all the C_T/σ tested and for C_T/σ greater than 0.058 is slightly positive (upload). These results demonstrate that reducing the wing incidence with respect to the wake flow (i.e. by rotating the outer portion of the wing), the wing behaves as a real aerodynamic body instead of a bluff body. The reason why the wing vertical load F_z^w resulted to be upward
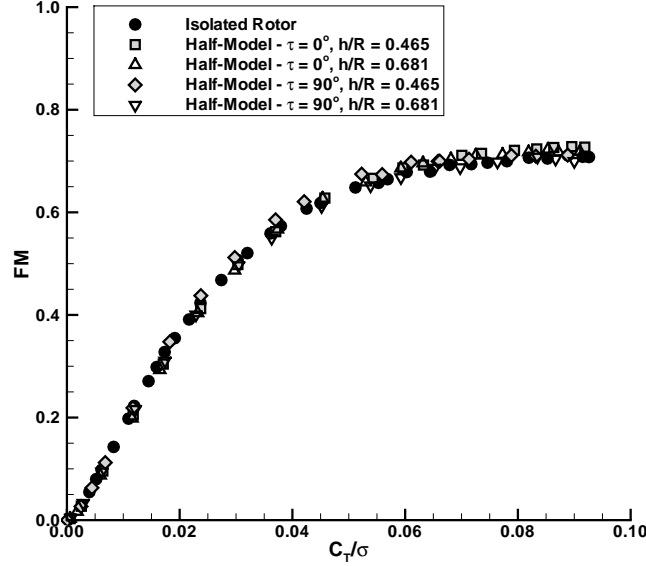
(a)
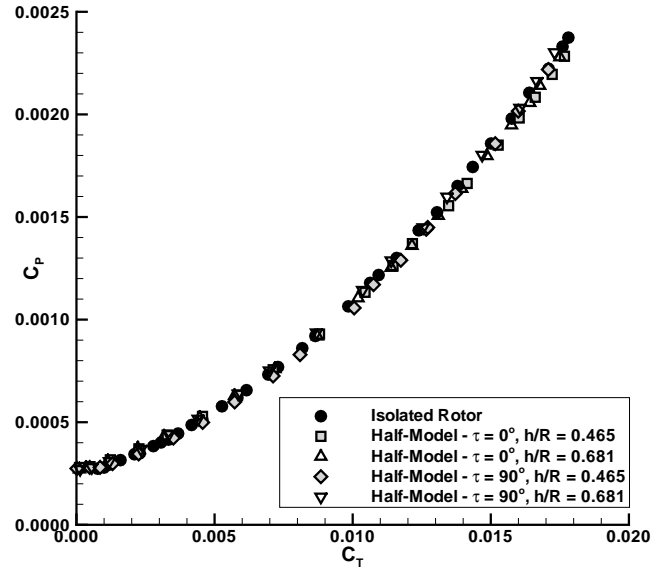
(b)

Figure 8: Comparison of rotor performance with tiltwing configurations, $M_{Tip} = 0.32$.

can be easily explained considering the wing sections effective angle of attack. In fact, in the tilted configuration, $\tau = 90°$, the outer part of the wing was set with the airfoil chord aligned vertically. Therefore a non-zero lift, normal to the relative local velocity can be expected due to the airfoil camber. The incidence induced by the rotor wake swirl further increases this local lift and orients it with a small upward component. In conclusion, in the tilted configuration the rotor performance is very similar to the one of the isolated rotor in hover. Even though this result is rather intuitive, it is still significant because quantitative information about this feature are not present in the past

literature. Actually, in the frame of the ERICA project[11], some experimental tests were carried out on half and full-span models but data were not made public.

For the tilted configuration, the measured longitudinal force acting on the wing is higher than vertical component and it is always positive, as it can deduced from Figure 9b showing the behaviour of the ratio between the F_x^w and the rotor thrust as a function of C_T/σ. In particular, for C_T/σ higher than 0.02 the longitudinal force/thrust ratio is nearly constant (about 4.5 %). Differently, in the untilted configuration the longitudinal force on the wing is almost zero. The measurements of non-negligible longitudinal force component acting on the wing in the tilted configuration demonstrates that, for the present hovering tests, the tiltwing model is not in a trimmed condition. The obtained results are related to the tilted wing configuration tested ($\tau = 90°$), that was assumed in this work as a reference condition. In fact, the presence of non-negligible longitudinal force component acting on the wing influences negatively the hovering flight but also may affect the conversion phase of the aircraft. Therefore, one of the goal to be considered during the design process of a tiltwing aircraft is to avoid the residual longitudinal force on the wing.

3.2 PIV measurements

PIV surveys were carried out both for the isolated rotor and for the half-model with the tilting wing set at $\tau = 90°$. In the latter configuration, the same two different wing-rotor distances ($h/R = 0.465$, $h/R = 0.681$) were considered. The collective blade pitch was $\theta = 12°$ and the rotor rotational speed was equal to 1120 rpm. Figure 10 shows the $r - \psi - z$ reference system adopted in the PIV measurements. Phase-locked PIV measurements were carried out from $\psi = 15°$ to $\psi = 90°$ with a 15° step. The measurements on each x-constant plane were phase-averaged over 100 image pairs.

Figure 11 shows the vorticity contours evaluated on the azimuthal measurement plane for the isolated rotor. The vorticity fields obtained for the different blade phases clearly show the progressive rotor wake contraction. In the upper part of Figure 11a the new generated vortex issued from the blade tip can be observed. With respect to this vortex, the one coming from the preceding blade is located sensibly closer to the rotor shaft but just slightly displaced in the vertical direction. The resulting induced velocity is clearly visible in Figure 12 where the radial distribution of the vertical velocity component U_z at several vertical positions below the rotor is shown. In the same figure, it can be observed that in the inner part of the rotor wake the vertical velocity accelerates from a minimum value of 15 m/s in the proximity of the rotor disk to a maximum of 19 m/s at $z/R = -0.35$.

The spatial location of the vortex cores, considered as the position of the vorticity peaks, highlights the rotor wake boundary, showing small changes between the different blade azimuthal positions. The
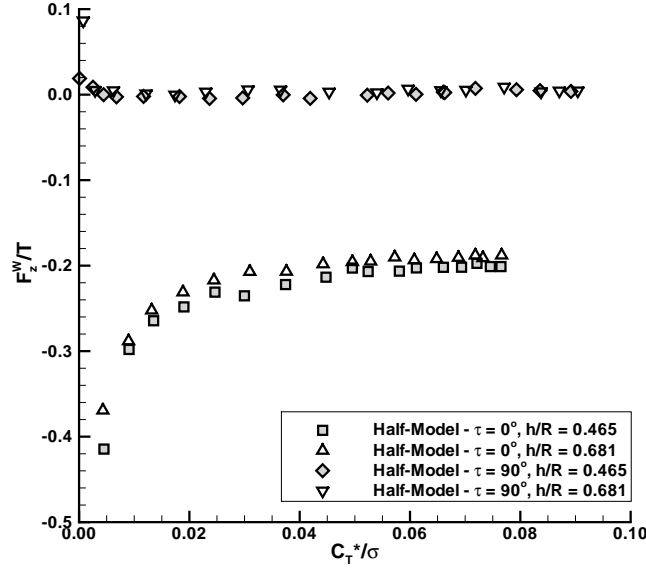
(a)
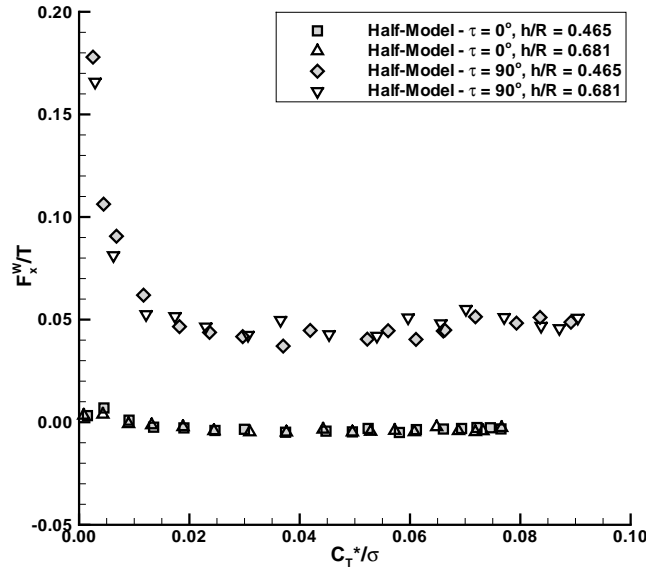
(b)

Figure 9: Half-wing airloads: (a) F_z^w/T as function of C_T/σ, (b) F_x^w/T as function of C_T/σ, $M_{Tip} = 0.32$.

maximum contraction of the wake is reached at an axial distance of $z/R \approx -0.4$. The evolution of the isolated rotor wake boundary can be quantitatively analysed in Figure 13 showing the tip vortex core displacements at the different blade azimuthal positions on $r - z$ plane. The radial position of the tip vortex core is rather constant after $z/R = -0.4$, thus the maximum contraction of the rotor wake assumes a radius of about $0.78\ R$. However, around $z/R = -0.5$ the wake boundary shows a local contraction that is apparent from $\psi = 30°$ to $\psi = 75°$. This sort of "kink" in the wake boundary profile
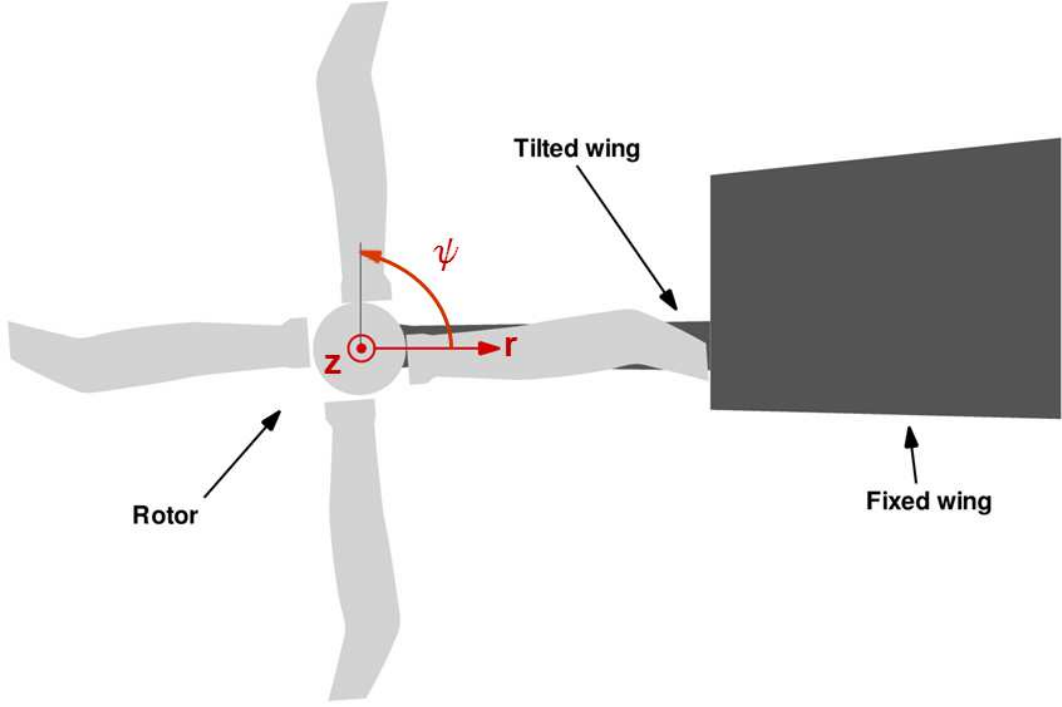
Figure 10: $r - \psi - z$ reference system adopted in the PIV measurements. The origin of the reference system is the same of the Cartesian $x - y - z$ system.

is due to the instability of the wake helical structure. In fact, this structure is characterised by an instability[28] that is basically the same instability of a 2D vortex array[29] producing the well-known phenomenon of vortex pairing. The vortex pairing is clearly visible in Figure 11 with the consequent production of the kink in the vortex-cores connecting lines of Figure 13. The same behaviour was observed by Darabi et al.[3] in the wake of the XV-15[1] rotor.

The phenomena observed for the isolated rotor case can be compared with the results obtained when the wing is introduced in the test rig. In particular, the PIV azimuthal surveys carried out for the isolated rotor can be directly compared with the PIV surveys on the x-constant window of half-model even if, due to its actual position ($x = -0.073 \ m$), this window does not strictly lie on an azimuthal plane. Furthermore, due to this x-shift an equivalent phase shift of about $5°$ has to be accounted in the comparison with the isolated rotor results.

For the lower wing position case (see Figure 14, where the tilted wing leading edge position is indicated by the dashed line) the wake boundary traced by the vortex cores is monotonically contracting till the wing leading edge position (indicated by the dashed line), where an early stage of the vortex pairing is observable, forced by the wing interference.
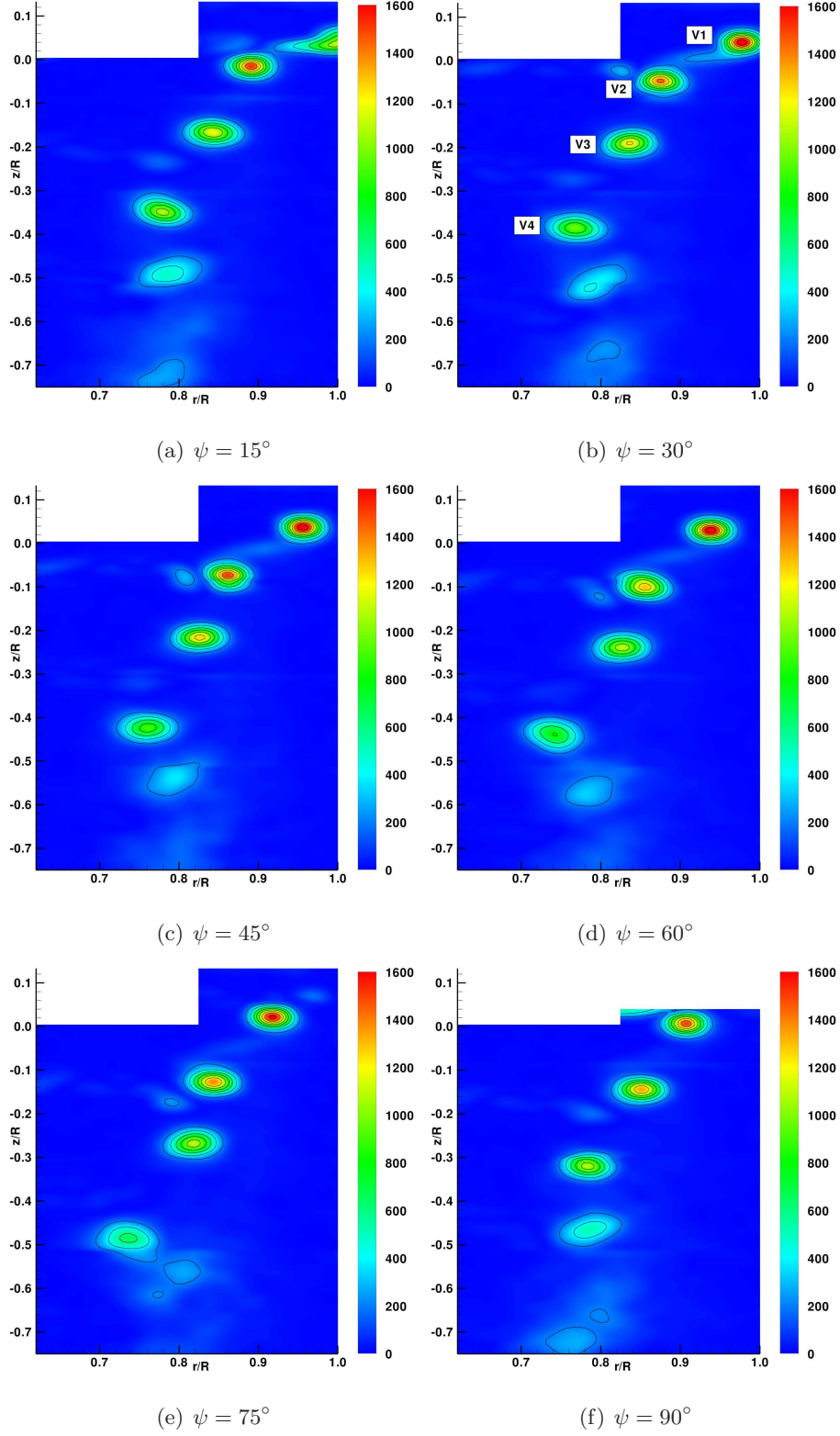
Figure 11: PIV results for isolated rotor: vorticity contours $[1/s]$

For the upper wing position case (see Figure 15), it is apparent that when the rotor wake is approaching the tilted wing, the presence of the wing prevents the natural wake contraction so that
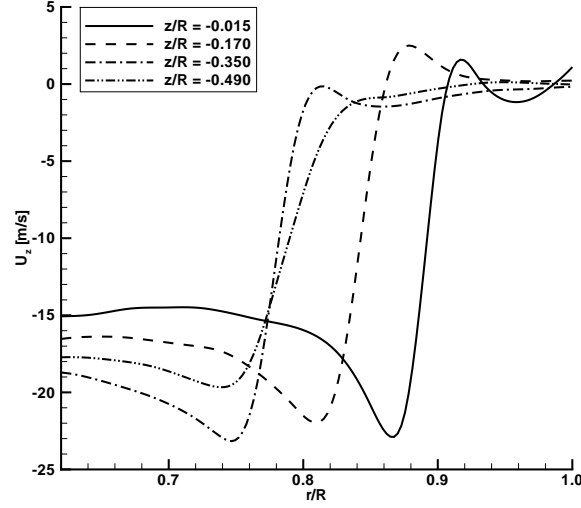
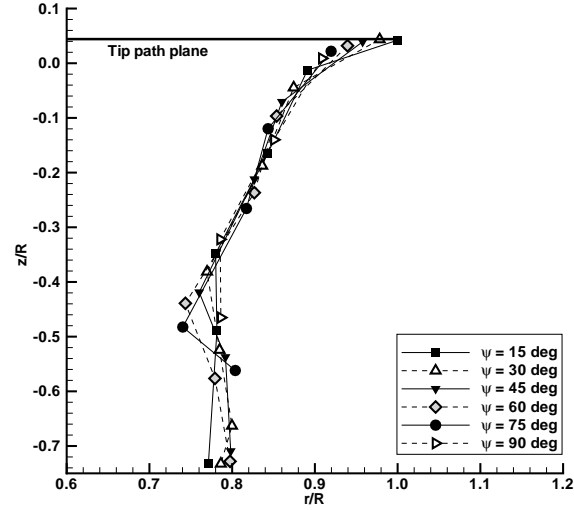Figure 12: Isolated rotor: U_z velocity component profiles, $\psi = 15°$.

Figure 13: Tip vortex core displacements in $r - z$ plane: isolated rotor wake boundaries at different blade azimuthal positions.

the minimum wake radius is larger than in the previous case. The U_z velocity profiles extracted for the azimuthal blade position $\psi = 15°$ (see Figure 16b) show an increase of the vertical velocity in the flow field region immediately below the leading edge of the wing ($z/R = -0.35$). This effect, that is probably due to the wing blockage, is not visible in the previous case (see Figure 16a) as in the lower position the wing leading edge projection lies just below the window lower boundary.

A quantitative comparison of the rotor wake boundary in the different configurations tested is presented in Figure 17 where, in order to improve the readability, the vortex core positions were
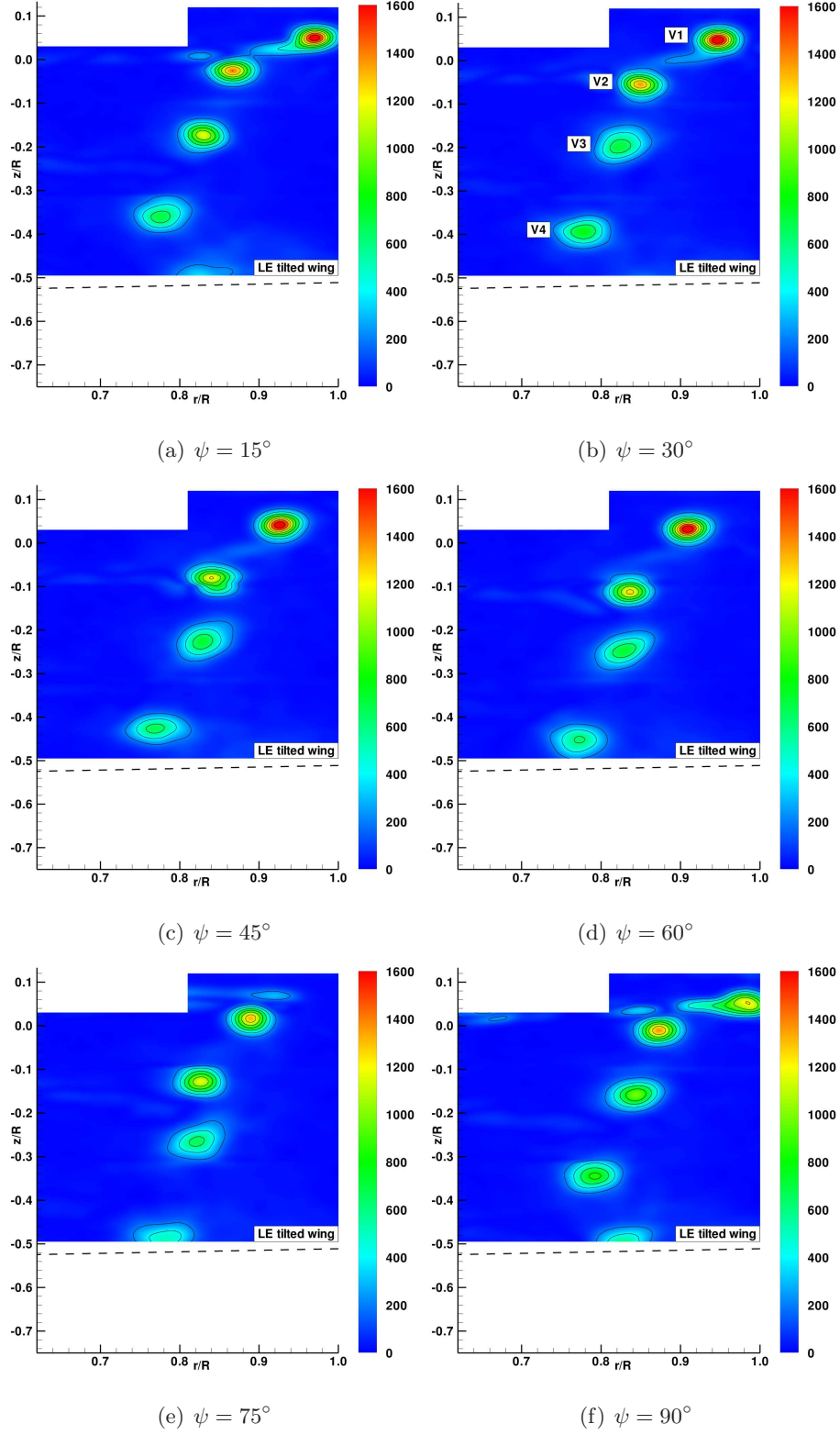
Figure 14: PIV results for half-model configuration, $\tau = 90°$, $h/R = 0.681$: vorticity contours $[1/s]$

plotted for all the phases together, so drawing the vortex traces on that plane. It is interesting to observe that the upper region of the rotor wake assumes the same shape for all the three analysed
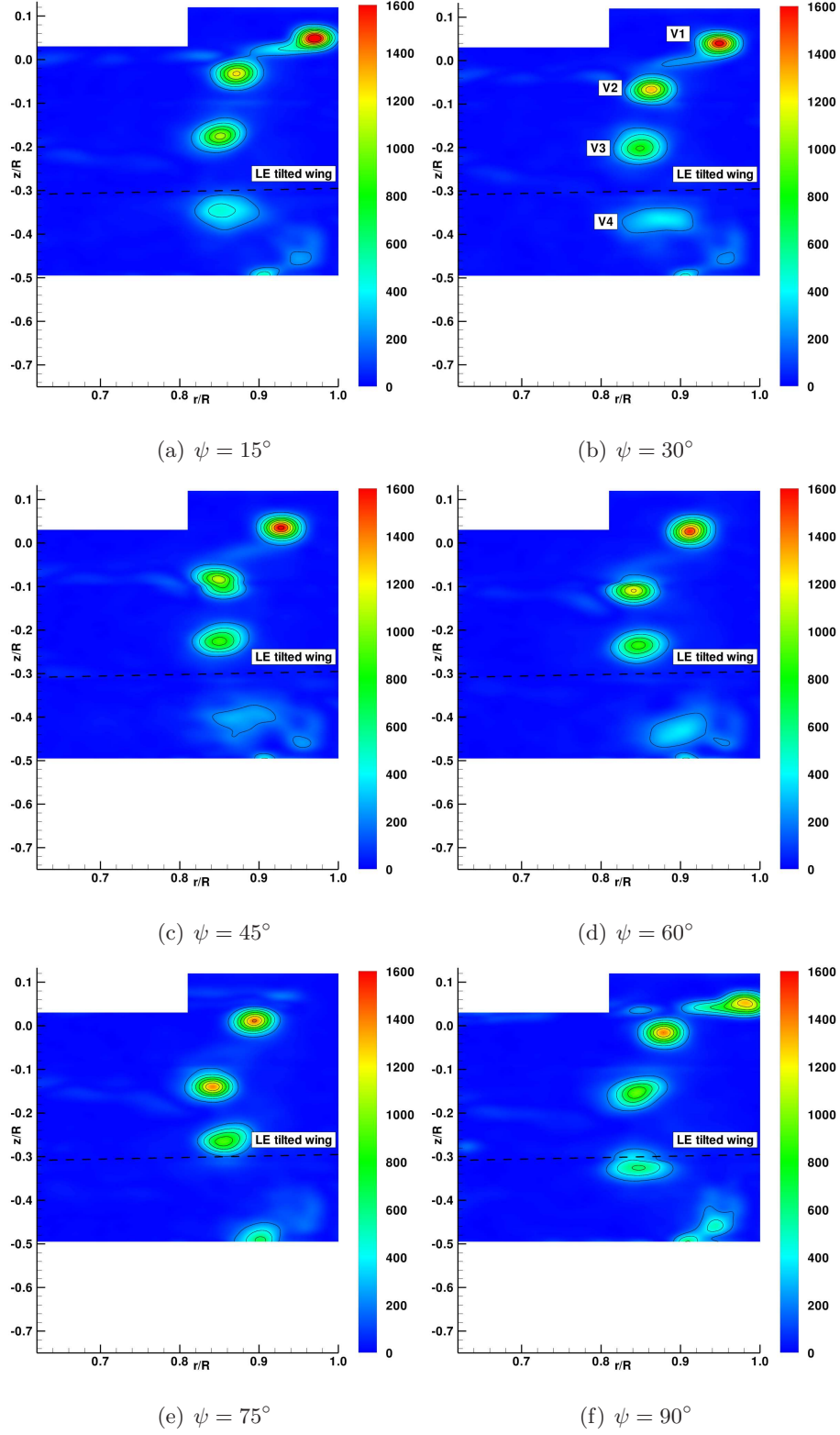
(a) $\psi = 15°$

(b) $\psi = 30°$

(c) $\psi = 45°$

(d) $\psi = 60°$

(e) $\psi = 75°$

(f) $\psi = 90°$

Figure 15: PIV results for half-model configuration, $\tau = 90°$, $h/R = 0.465$: vorticity contours $[1/s]$

cases. This behaviour is probably due to the small blockage effect produced by the tilted portion of the wing spanning all the rotor wake. The wake obtained with the wing in the lower position has a
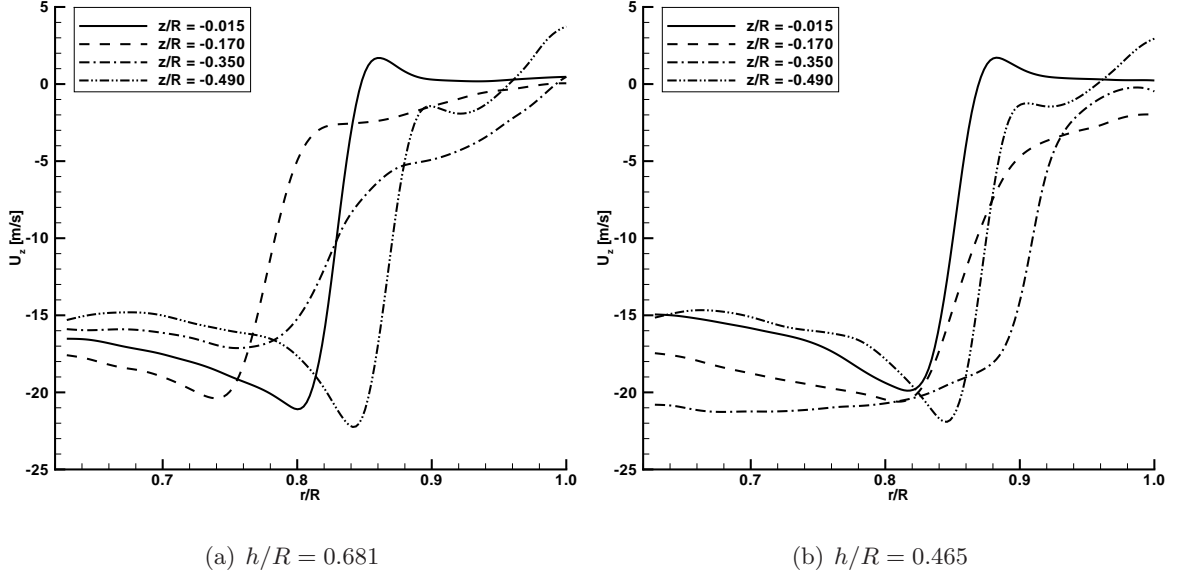
(a) $h/R = 0.681$　　　　　　　　　(b) $h/R = 0.465$

Figure 16: Half-model, $\tau = 90°$, $\psi = 15°$: U_z velocity component profiles.

profile quite similar to the isolated rotor case except for the region just above the wing. In fact, in this flow area the isolated rotor wake exhibits the previously described kink while for the lower wing position case the wake enlargement due to the wing is apparent. For the upper wing position case, the maximum contraction of the rotor wake is observed at $z/R = -0.14$ with a radius of about 0.85 R, thus sensibly larger than the value of about 0.8 R obtained for the lower wing position case.

In Figure 18 the standard deviation of the vortex centre positions evaluated over all the 100 instantaneous velocity fields obtained by the 100 PIV image pairs is shown for the azimuthal blade position $\psi = 30°$. The statistical analysis was carried out for the four vortices identified in Figure 11b, 14b and 15b by V1, V2, V3 and V4. The disturbance effect produced by the wing is particularly apparent. In fact, the maximum variability is exhibited by the vortex V4 when the wing is in the upper position ($h/R = 0.465$) so that this vortex is in the wing leading edge region. It has to be pointed out that the small delay exhibited by the vortices of the isolated rotor in the figure is illusory because the measurement planes for the half-model cases are slightly shifted for reasons of optical accessibility, as described in section 2.2. The high variability of the lowest vortex position for the upper wing case ($h/R = 0.465$) is the main cause of the remarkable diffusion observed in Figure 15b. This effect is clearly visible by comparing the velocity profiles extracted by the mean flow through the vortex core with the mean velocity profiles of the actual instantaneous vortices. The latter profiles were obtained by averaging the 100 instantaneous velocity flow fields previously shifted in order to refer the coordinate system to corresponding instantaneous vortex centres (see Figure 19). In conclusion, the strong spread observed for the lowest vortex (V4) when the wing is in the upper position is essentially

a wandering effect[30] more than a real diffusion of the vortex core.
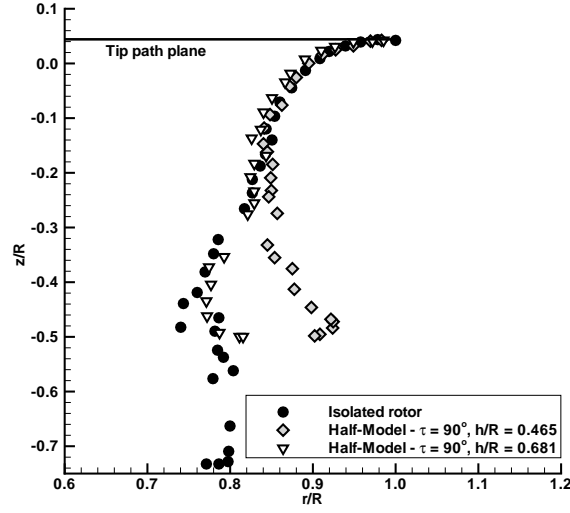

Figure 17: Tip vortex core displacements: comparison between the isolated rotor and the half-model tilted wing configurations.
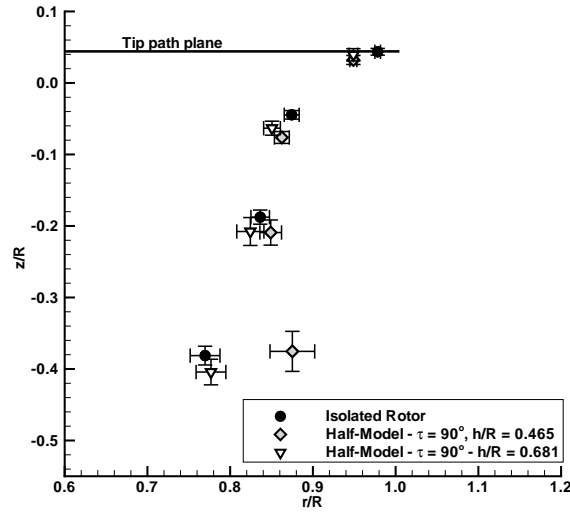

Figure 18: Tip vortex core displacements variability: comparison between the isolated rotor and the half-model tilted wing configurations at $\psi = 30°$.

The PIV measurements on the y-constant planes, carried out for the upper wing case only, allow to analyse the flow impinging on the wing sections. Figure 20 shows the time-averaged PIV results illustrated by means of U_x velocity component contours and in-plane streamlines. The streamlines patterns show that the tilted wing section experiences a positive angle of attack induced by the contribution of the rotor wake swirl. The observed flow field confirms the considerations about the
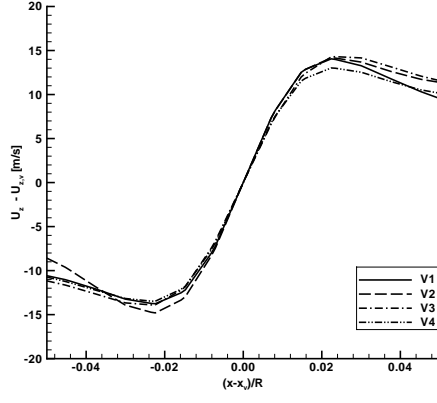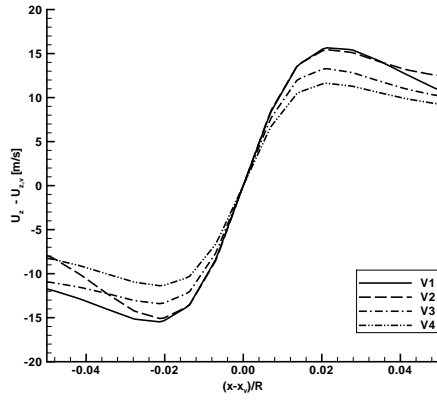
(a) Isolated rotor, mean of instantaneous vortices
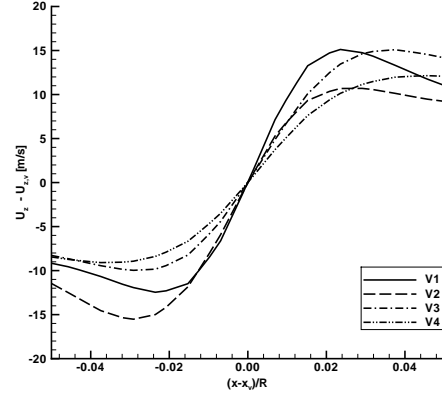
(b) Isolated rotor, mean flow vortices

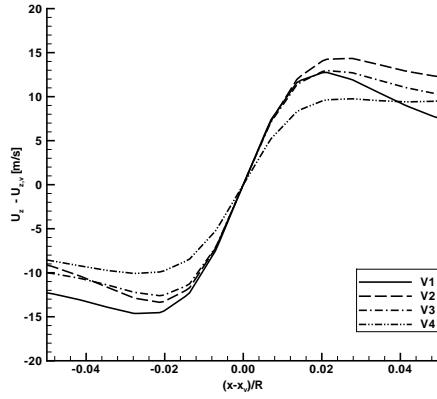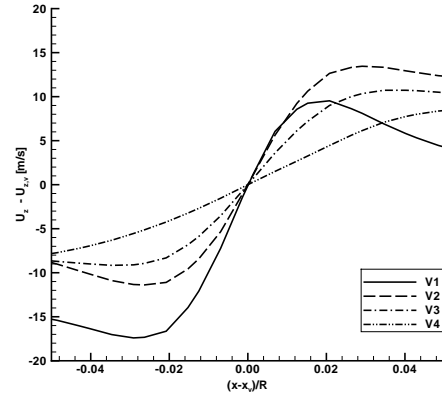(c) Half-model $h/R = 0.681$, mean of instantaneous vortices
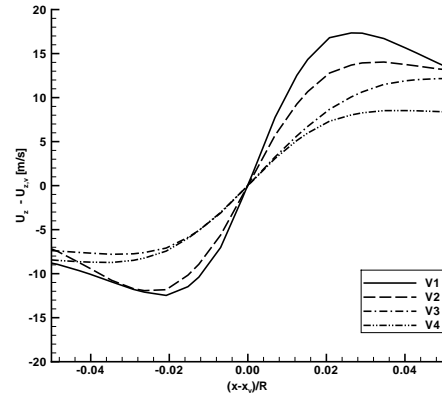
(d) Half-model $h/R = 0.681$, mean flow vortices

(e) Half-model $h/R = 0.465$, mean of instantaneous vortices

(f) Half-model $h/R = 0.465$, mean flow vortices

Figure 19: U_z velocity component profiles through the vortex cores at $\psi = 30°$. For the vortices numbering see Figure 11b, 14b and 15b

airloads measured on the half-wing in this configuration (see Figure 9). A quantitative analysis of this feature is provided by Figure 21 showing the mean profiles of the U_x and U_z velocity components extracted in correspondence of the tilted wing leading edge. The U_x component (corresponding to the rotor wake tangential velocity component) is rather constant in the inner measurement plane ($y/R = 0.69$), with a value of about 3 m/s, while in the outer plane ($y/R = 0.79$) it varies from a minimum value of 1 m/s to a peak of 3 m/s at $z/R = -0.23$ (see Figure 21a). On the other hand, the peaks of the measured mean U_z are respectively 15 m/s and 19 m/s in the inner and outer measurement planes (see Figure 21b). The induced local angle of attack estimated considering the mean values of the U_x and U_z measured at the leading edge region is close to 11° in the inner plane and to 9° in the outer plane. These values are compatible with the loads measured on the half-wing in this test condition.

(a) $r/R = 0.69$ (b) $r/R = 0.79$
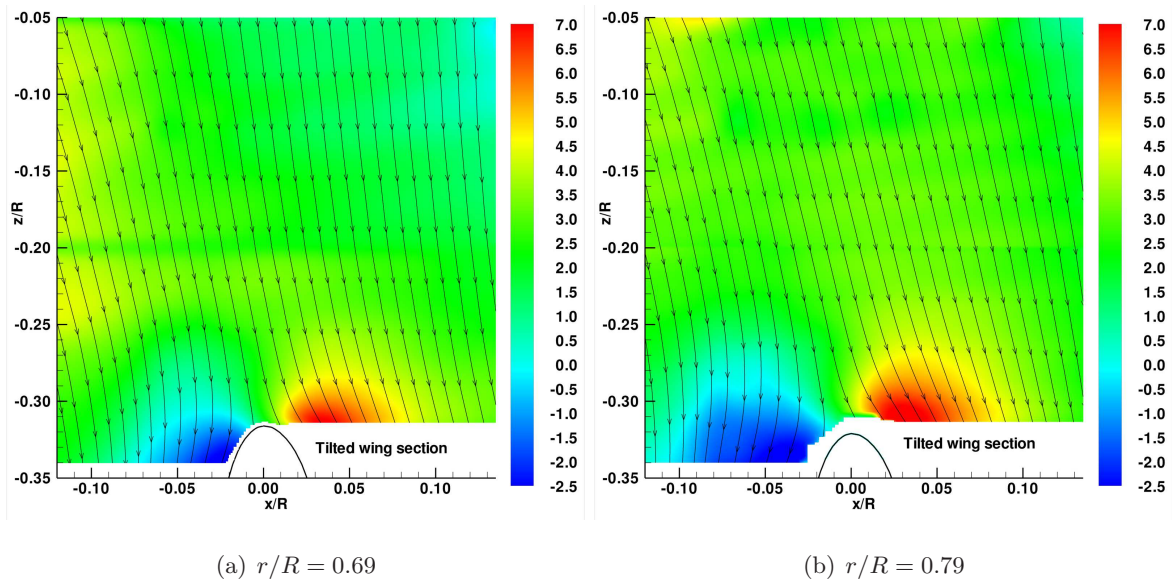
Figure 20: PIV results for half-model configuration on radial planes, $\tau = 90°$, $h/R = 0.465$: U_x velocity component contours $[m/s]$ and in-plane streamlines.

4   Conclusions

The present work described the results of an experimental activity carried out on a tiltwing aircraft half-model to achieve a detailed investigation of the main phenomena related to the aerodynamic interaction between wing and rotor in hover. The use of different reliable experimental techniques as loads measurements and PIV enabled to study both the performance of this aircraft configuration and the flow field between rotor and wing. Thanks to the modularity of the half-model, the performance

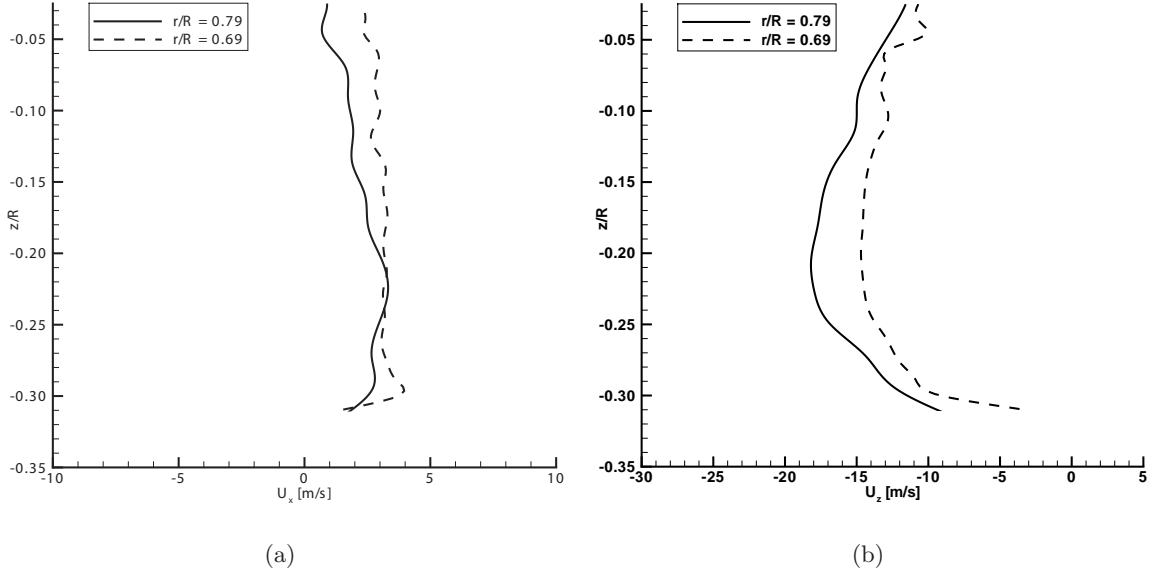Figure 21: Half-model, $\tau = 90°$, $h/R = 0.465$, $\psi = 15°$: (a) U_x and (b) U_z mean velocity component profiles extracted in correspondence of the tilted wing leading edge.

of the isolated rotor was first characterised to be compared with the results obtained with the wing. In particular, considerations from the analysis of the experimental results include the following:

1. The measurements of the rotor and wing airloads enabled to quantitatively analyse the performance of the aircraft system and of the rotor. In particular, the experimental results show that the tilting of a wing portion spanning all the rotor wake is enough to improve the total system performance. This improvement is mainly due to the cancellation of the wing download effect while the rotor performance is not remarkably influenced by the wing even though a slight improvement is observed for the untilted configuration due to a partial ground effect.

2. The obtained results did not highlight any sensible difference in the performance related to the two considered wing vertical positions. This insensibility to the wing-rotor distance (at least in the range considered) leaves this parameter free to be adjusted for other goals.

3. The measurements of the wing airloads showed a small upload although in the presence of a non-negligible horizontal force that should be taken into account for the global equilibrium of the aircraft.

4. The PIV surveys enabled to achieve a detailed insight about the flow physics of the rotor wake in the interaction with the wing. In particular, the phase-locked PIV measurements carried out at different blade azimuthal positions illustrated the extent of the rotor wake boundary

as well as the evolution of the spatial displacement of the tip vortex influenced by the vortex pairing. In fact, for the higher wing position it was observed that the interaction with the tilted wing influences the contraction of the rotor wake with respect to the isolated rotor case. The quantification of wake contraction size could be used in the aircraft design making the tilting wing span to fit the actual wake size.

5. A statistical analysis of the vortex positions showed a remarkable variability when the tip vortex approaches the wing leading edge region. This vortex wandering produces an illusory high diffusion of the vortex core if just the mean flow field is observed.

6. The PIV measurements carried out on different radial planes near the wake rim enabled to obtain quantitative information about the rotor wake swirl for the half-model configuration with the tilted wing.

The comprehensive experimental database, obtained over a not confidential aircraft configuration, can be considered an important contribution for the study of the tiltwing aircraft configurations. In particular, in order to allow a CFD analysis of the tested aircraft configuration, the experimental database and the detailed description of the test rig set up are accessible by request to the authors.

References

1. Maisel, M., Giulianetti, D., and Dugan, D., The history of the XV–15 tilt rotor research aircraft: from concept to flight, Monographs in Aerospace History, 17 SP-2000-4517, NASA History Division, 2000.

2. Gazdag, D. and Altonin, L., Potential use of tiltrotor aircraft in Canadian aviation, Technical Report TM-102245, NASA Technical Memorandum, 1990.

3. Darabi, A., Stalker, A., McVeigh, M., and Wygnanski, I., The Rotor Wake Above a Tiltrotor Airplane-Model in Hover, 33rd AIAA Fluid Dynamics Conference, Orlando, Florida, USA, 23-26 June 2003.

4. McVeigh, M. A., The V-22 Tiltrotor Large–Scale Rotor Performance/Wing Download Test and Comparison With Theory, *Vertica*, Vol. 10, (3/4), 1986, pp. 281-297.

5. Felker, F. and Light, J. S., Aerodynamic Interactions Between a Rotor and Wing in Hover, *Journal of the American Helicopter Society*, April 1988, pp. 53-61.

6. McCluer, M. and Johnson, J., Full-Span Tiltrotor Aeroacoustic Model (FS TRAM). Overview and Initial Testing, American Helicopter Society Aerodynamics, Acoustics, and Test and Evaluation Technical Specialists Meeting, San Francisco, CA, USA, 23-25 January 2002.

7. Johnson, W., Calculation of Tilt Rotor Aeroacoustic Model (TRAM DNW) Performance, Airloads, and Structural Loads, American Helicopter Society Aeromechanics Specialists Meeting, Atlanta, Georgia, USA, November 2000.

8. Felker, F., Wing Download Results from a Test of a 0.658-Scale V-22 Rotor and Wing, *Journal of the American Helicopter Society*, Vol. 37, (4), October 1992, pp. 58-63.

9. McVeigh,M., Grauer,W., and Paisley, D., Rotor/Airframe Interaction On Tiltrotor Aircraft, *Journal of American Helicopter Society*, Vol. 35, (3), July 1990, pp. 43-51.

10. Polak, D., Rehm, W., and George, A., Effects of an Image Plane on the Tiltrotor Fountain Flow, *Journal of American Helicopter Society*, Vol. 45, (2), April 2000, pp. 90-96.

11. Alli, P., Nannoni, F., and Cicalè, M., ERICA: The european tiltrotor design and critical technology projects, International Air and Space Symposium and Exposition: The Next 100 Years, Dayton, Ohio, USA, 14–17 July 2005.

12. Gupta, V. and Baeder, J. D., Investigation of Quad Tiltrotor Aerodynamics in Forward Flight Using CFD, 20th AIAA Applied Aerodynamics Conference, St. Louis, MO, USA, 24–26 June 2002.

13. Lefebvre, T., Beaumier, P., Canard-Caruana, S., Pisoni, A., Pagano, A., Sorrentino, A., der Wall, B. V., Yin, J., Arzoumanian, C., Voutsinas, S., and Hermans, C., Aerodynamic and aero-acoustic optimization of modern tilt-rotor blades within the ADYN project, 4th European Congress on Computational Methods in Applied Sciences and Engineering, Jyvaskyla, Finland, 24–28 July 2004.

14. Decours, J., Burguburu, S., and Falissard, F., Performance Assessment of the Erica Tilt-Rotor in Cruise, 36th European Rotorcraft Forum, Paris, France, 7–9 September 2010.

15. Droandi, G., Gibertini, G., and Biava, M., Wing-Rotor Aerodynamic Interaction in Tiltrotor Aircraft, 38th European Rotorcraft Forum, Amsterdam, The Netherlands, 4-7 September 2012.

16. Droandi, G., Gibertini, G., Lanz, M., Campanardi, G., and Grassi, D., Wing-Rotor Interaction On A 1/4-Scale Tiltrotor Half–Model, 39th European Rotorcraft Forum, Moscow, Russia, 3–6 September 2013.

17. Gibertini, G., Auteri, F., Campanardi, G., Macchi, C., Zanotti, A., and Stabellini, A., Wind tunnel tests of a tilt-rotor aircraft, The Aeronautical Journal, Vol. 115, (1167), May 2011, pp. 315-322.

18. Beaumier, P., Decours, J., and Lefebvre, T., Aerodynamic and Aeroacoustic Desing of Moder Tilt-Rotors: the Onera Experience, 26th International Congress of the Aeronautical Sciences, Anchorage, Alaska, USA, 14-19 September 2008.

19. Grife, A., Darabi, A., and Wygnanski, I., Download Reduction on a Three Dimensional V-22 Model Using Active Flow Control, 1st AIAA Flow Control Conference, St. Louis, Missouri, USA, June 24-26 2002.

20. Droandi, G., Wing–Rotor Aerodynamic Interaction in Tiltrotor Aircraft, Ph.D. thesis, Politecnico di Milano, 2014.

21. Droandi, G. and Gibertini, G., Aerodynamic Blade Design with Multi-Objective Optimization for a Tiltrotor Aircraft, *Aircraft Engineering and Aerospace Technology*, Vol. 87, N. 1, 2015, pp. 19-29.

22. Abbott, I. and Doenhoff, A. V., Theory of Wing Sections, Including a Summary of Airfoil Data, McGraw-Hill Book Co., Inc. (Reprinted by Dover Publications, 1959), 1949.

23. L.K. Loftin, J., Theoretical and Experimental Data for a Number of NACA 6A-Series Airfoil Section, Technical Report TR-903 (Supersedes NACA TN-1368), NACA, 1948.

24. Zanotti, A., Grassi, D., and Gibertini, G., Experimental investigation of a trailing edge L-shaped tab on a pitching airfoil in deep dynamic stall conditions, *Proc of IMechE, Part G: Journal of Aerospace Engineering*, Vol. 228, N. 12, 2014, pp. 2371-2382.

25. PIVTEC, PIVview 2C version 3.0. User manual, www.pivtec.com, January 2009.

26. Raffel, M., Willert, C., and Kompenhans, J., Particle Image Velocimetry, a practical guide, Springer, 1998.

27. Young, L., Lillie, D., McCluer, M., Yamauchi, G., and Derby, M., Insights into Airframe Aerodynamics and Rotor-on-Wing Interactions from a 0.25–Scale Tiltrotor Wind Tunnel Model, American Helicopter Society Aerodynamics, Acoustics, and Test and Evaluation Technical Specialists Meeting, San Francisco, CA, USA, 23-25 January 2002.

28. Bhagwat, M. and Leishman, G., On the Aerodynamic Stability of Helicopter Rotor Wakes, *AIAA Journal*, Vol. 38, (2), 2000, pp. 301-308.

29. Metcalfe, R., Orszag, S., Brachet,M.,Menon, S., and Riley, J., Secondary instability of a temporally growing mixing layer, *Journal of Fluid Mechanics*, Vol. 184, 1987, pp. 207-243.

30. Gibertini G., Mencarelli A., Zanotti A., Oscillating Aerofoil and Perpendicular Vortex Interaction, *Proc of IMechE, Part G: Journal of Aerospace Engineering*, Vol. 228, N. 6, 2014, pp. 846-858.